Wave-packet dynamics on Chern-band lattices in a trap

Sthitadhi Roy, Adolfo G. Grushin, Roderich Moessner, and Masudul Haque
Max-Planck-Institut für Physik Komplexer Systeme, Nöthnitzer Straße 38, 01187 Dresden, Germany
(Received 30 September 2015; published 17 December 2015)

The experimental realization of lattices with Chern bands in ultracold-atom and photonic systems has motivated the study of time-dependent phenomena, such as spatial propagation, in lattices with nontrivial topology. We study the dynamics of Gaussian wave packets on the Haldane honeycomb Chern-band lattice model, in the presence of a harmonic trap. We focus on the transverse response to a force, which is due partly to the Berry curvature and partly to the transverse component of the energy band curvature. We evaluate the accuracy of a semiclassical description, which treats the wave packet as a point particle in both real and momentum space, in reproducing the motion of a realistic wave packet with finite extent. We find that, in order to accurately capture the wave-packet dynamics, the extent of the wave packet in momentum space needs to be taken into account: The dynamics is sensitive to the interplay of band dispersion and Berry curvature over the finite region of momentum (reciprocal) space where the wave packet has support. Moreover, if the wave packet is prepared with a finite initial momentum, the semiclassical analysis reproduces its motion as long as it has a large overlap with the eigenstates of a single band. The semiclassical description generally improves with increasing real-space size of the wave packet, as long as the external conditions (e.g., external force) remain uniform throughout the spatial extent of the wave packet.

DOI: 10.1103/PhysRevA.92.063626 PACS number(s): 67.85.−d, 03.75.Lm, 03.65.Sq, 03.65.Vf

I. INTRODUCTION

The presence of nontrivial topology in the energy bands of lattice models [1,2] has generated intense interest over the past decade. When an energy band possessing a nonzero Chern number is filled with fermions, one obtains a Chern insulator, realizing a quantized Hall effect without external magnetic fields. The Chern number is a topological invariant, defined as the flux of the Berry curvature over the Brillouin zone. The Berry curvature acts like a momentum-space analog of the magnetic field [3]. One of the first examples of a Chern-band model was introduced in the seminal work by Haldane [4], where time-reversal symmetry is explicitly broken in a honeycomb lattice model of free fermions by complex hoppings between next-nearest-neighbor lattice sites.

Chern-band physics has been discussed in numerous different scenarios. Originally, the focus was on electronic systems [5–9]. More recently, lattices with nontrivial Berry curvature have been experimentally realized using ultracold atoms trapped in optical lattices [10–13]. The spatial geometries in these setups are more flexible than in traditional solid-state situations. These experimental developments have thus motivated the study of effects of lattice and trap geometries on topological states [14–19]. Cold atoms also provide an excellent platform for observing and analyzing nonequilibrium dynamics of Chern bands. Therefore, there has been increasing interest in developing protocols to characterize the topological nature of Chern bands from nonequilibrium behavior [20–30]. For instance, the quench dynamics of Chern insulators can signal their nontrivial edge states [26] and the semiclassical trajectory of wave packets can be related to the Chern number [22].

Topological photonics has proved itself to be another important context for Chern-band physics [31–40]. Theoretical studies and proposals [32–36] have also been supplemented by experimental observation of the topological edge states in photonic systems [37–40]. In addition, topological magnons have been proposed as a platform to study transport influenced by Berry curvature in the context of the thermal Hall effect [41–43].

For ultracold atoms (especially bosons) and for photonic systems, a dynamical situation where the atoms or photons form a spatially localized and evolving wave packet is more natural than a static situation in which a band is exactly filled. Thus, the recent experimental developments call for a systematic understanding of the nonequilibrium dynamics of realistic wave packets on Chern-band models. A particularly important theme is the response of a localized wave packet to an applied force (potential gradient) [13,22,27,29,44]. One expects Bloch oscillations in the direction of the applied force. In addition, there is also motion perpendicular to the direction of the force, with contributions due to the topological Berry curvature and due to the band dispersion.

A natural framework to describe the motion of wave packets is to use semiclassical equations of motion. For systems with Berry curvature, the semiclassical equations were introduced in the context of crystals with magnetic Bloch bands [45–50], anomalous Hall responses [50–52], and optical lattices with spin-orbit coupling [53]. They have been used to study the effect of the Berry curvature on wave-packet trajectories [29,54] and on collective modes [55,56] in ultracold gases. For instance, Ref. [29] outlines a procedure to isolate the contribution of the topological Berry curvature by separately evolving the system under opposite potential gradients and then appropriately summing up the responses.

Semiclassical approaches typically rely on the approximation of assigning a sharply defined position and momentum simultaneously to a quantum state. Based on this assumption one can solve the set of coupled differential equations for position and momenta and hence obtain sharply defined trajectories of the particle in both real and momentum space.

However, this assumption is *a priori* not valid in realistic situations where the wave packets have a finite spread in both real and momentum space, a scenario expected in typical ultracold bosonic and photonic experiments.

In this work we study the effect of size and initial momentum of a wave packet placed off center in a harmonic trap in Haldane's honeycomb model and evaluate the ability of the semiclassical approach to describe these effects. We focus on time evolutions up to moderate time scales such that the displacement of the wave packet from its initial position is not large compared to the wave-packet size and much smaller than the distance to the center of the trap. In this regime the trap plays a role similar to a constant force. We quantify the transverse motion of the wave packet using the angular velocity $\dot{\theta}$ with respect to the center of the trap.

We find that the standard point-particle semiclassical approach captures some qualitative features of the dynamics, but is generally insufficient to quantitatively describe the actual real-time dynamics. Therefore, we reformulate the semiclassical description to take into account the finite spread of the wave packet in momentum space. The exact evolution of $\dot{\theta}$ is compared in detail to predictions from the extended semiclassics and from the standard point-particle semiclassics. In momentum space the wave packet moves at a constant rate in the direction of the force, leading to Bloch oscillations. As it crosses different regions of the Brillouin zone, the local Berry curvature and band curvature determine $\dot{\theta}(t)$. For spatially localized wave packets, the extent in momentum space is finite. The extended semiclassics procedure incorporates the variations of band dispersion and Berry curvature in this extended region of momentum space. We find that, as long as the physics is dominated by one band, this procedure reproduces the full dynamics well. This shows that the basic idea of semiclassics (simultaneously assigning both position and momentum to a quantum particle) can incorporate aspects of the full quantum dynamics to an extent beyond what is known from the usual point-particle treatment.

One might intuitively expect that semiclassical descriptions should work better for spatially large wave packets since these correspond to smaller regions in momentum space. We show that this is generally true, but that semiclassics still describes the dynamics of rather small wave packets, especially if momentum-space extent is included. In addition, by considering a tight trap, we show an example of possible experimental relevance where larger real-space sizes can render the semiclassical description less inaccurate, due to an inhomogeneity of the force within the spatial support region of the wave packet.

We also demonstrate the effect of initializing the wave packet with a finite momentum. In addition to zero momentum (Γ point) we start with the packet at one of the **K** points and one of the **M** points of the Brillouin zone. We show that imparting momenta to a Gaussian wave packet using an $e^{i\mathbf{k}\cdot\mathbf{r}}$-like factor can cause the wave function to have significant occupancy in the upper band, including extreme cases where it is almost completely transferred to the upper band. As long as one of the bands dominates, the semiclassical description works well when using the properties (band dispersion and Berry curvature) of the band where the state has most of its weight. The single-band semiclassical procedure is naturally insufficient when multiple bands are significantly occupied: Features such as interference oscillations are not captured by an incoherent averaging of contributions from different bands.

The rest of the paper is organized as follows. In Sec. II we describe the model, the geometries, and the simulations of time evolution. In Sec. III we discuss the semiclassical framework for the dynamics of the wave packet, followed by a comparison of the results from simulations and semiclassics in Sec. IV. Finally, we comment on the dynamics in a tight harmonic trap in Sec. V and provide some discussion and context in Sec. VI.

II. SIMULATIONS OF WAVE-PACKET DYNAMICS ON THE HALDANE MODEL

A. Model Hamiltonian

Haldane's model [4] is a tight-binding Hamiltonian on a honeycomb lattice

$$\mathcal{H}_{\mathrm{HM}} = J_1 \sum_{\langle i,j\rangle} \hat{b}_i^\dagger \hat{b}_j + J_2 \sum_{\langle\langle i,j\rangle\rangle} e^{i\phi_{ij}} \hat{b}_i^\dagger \hat{b}_j + \mathrm{H.c.}, \qquad (1)$$

where the $\langle i,j\rangle$ denotes the nearest neighbors, $\langle\langle i,j\rangle\rangle$ denotes the next-nearest neighbors, and $\hat{b}_j^\dagger$ ($\hat{b}_j$) is the creation (annihilation) operator at site i. We will formally consider the dynamics of a single particle, so $\hat{b}_j^\dagger$ and $\hat{b}_j$ may be thought of as either fermionic or bosonic operators. When particles hop between next-nearest neighbors they pick up a phase $\phi_{ij} = \phi$ if they hop in the direction of the arrow shown in Fig. 1(a) and $-\phi$ if they hop in the opposite direction. The energy spectrum is gapped if $\phi \neq n\pi$ and is particle hole symmetric for $\phi = \pi/2$. Throughout this paper we use the parameters

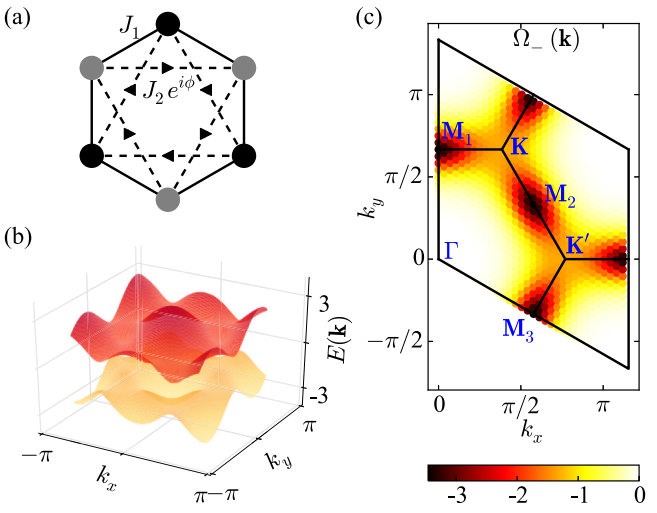

FIG. 1. (Color online) (a) Honeycomb lattice defining the Haldane model (1) with black and gray circles denoting the two sublattices. The solid lines represent the real nearest-neighbor hoppings and the dotted lines the complex next-nearest-neighbor hoppings. The arrows indicate the direction in which the particle hops to pick up a phase ϕ. (b) Two-band energy spectrum with parameters $J_1 = -1$, $J_2 = -1/4$, and $\phi = 0.49\pi$. (c) Berry curvature in the lower band for the same parameter values shown as a color map in the Brillouin zone. The high symmetry points are marked. The boundaries of the Brillouin zone are formed by the reciprocal lattice vectors $\mathbf{G}_1 = (0, 4\pi/3)$ and $\mathbf{G}_2 = (2\pi/\sqrt{3}, -2\pi/3)$.

$J_1 = -1$, $J_2 = -1/4$, and $\phi = 0.49\pi$, for which the energy spectrum is depicted in Fig. 1(b). The parameters are chosen so that the two energy bands are quite similar and none of them are excessively flat (since band flatness can introduce additional peculiarities in the dynamics) and so as to avoid exact particle-hole symmetry, since we are interested in generic rather than fine-tuned effects. We expect the physics described in this paper (explicitly for these parameters) to be exemplary for a wide region in parameter space.

For these parameters the bands have a finite Chern number: -1 for the lower band and $+1$ for the upper band. The distribution of the Berry curvature of the lower band in the Brillouin zone is shown in Fig. 1(c). The upper band has approximately opposite Berry curvature, i.e., positive instead of negative values. We provide some details of the topological properties and conventions in the Appendix. Figure 1(c) also shows the high-symmetry points. In addition to zero momentum (Γ point), these are three inequivalent $\mathbf{M}$ points and two inequivalent $\mathbf{K}$ points. We choose the boundaries of the Brillouin zone to be a parallelogram. In the literature this is equivalently often chosen to be of hexagon shape; the solid lines inside the Brillouin zone show the boundaries for such a choice.

We set $\hbar = 1$, measuring time in units of $\hbar/J_1$ and energy in units of J_1. Space and momentum are in units of lattice spacing (set to unity) and inverse lattice spacing, respectively, and geometric angles are measured in radians.

B. Construction of wave packets

We are interested in the dynamics of a wave packet of finite real-space extent in Haldane's honeycomb model in the presence of a harmonic trap. The initial wave packet is prepared with a Gaussian shape. For zero initial momentum,

$$|\psi(t=0)\rangle = \frac{1}{\mathcal{N}}\sum_l c_l|l\rangle = \frac{1}{\mathcal{N}}\sum_l e^{-\frac{|\mathbf{r}_l-\mathbf{r}_c|^2}{2\sigma^2}}|l\rangle. \quad (2)$$

Here $|l\rangle$ denotes a single-particle state, with the particle completely localized at a site indexed by l, $\mathcal{N}$ is a normalization factor, and $\mathbf{r}_l = (x_l, y_l)$ denotes the Euclidean position of site l. The coefficient $c_l(t)$ denotes the amplitude of the wave function at time t at site l and σ is the width of the wave packet. We will also use wave packets with nonzero initial momenta. A finite momentum is obtained by multiplying the coefficients with a site-dependent phase factor

$$\begin{aligned}|\psi(t=0;\mathbf{k}_0)\rangle &= \sum_l c_{l,0}e^{i\mathbf{k}_0\cdot\mathbf{r}_l}|l\rangle \\ &= \frac{1}{\mathcal{N}}\sum_l \exp\left[-\frac{|\mathbf{r}_l-\mathbf{r}_c|^2}{2\sigma^2}+i\mathbf{k}_0\cdot\mathbf{r}_l\right]|l\rangle.\end{aligned} \quad (3)$$

In cold-atom experiments, a wave packet or atomic cloud can be boosted in momentum space in this way using a Bragg pulse; this is commonly used to determine the excitation spectrum of cold-atom systems using Bragg spectroscopy (see, e.g., Ref. [57] for a description of the experimental technique). In experimental spectroscopy, both energy and momentum are well resolved in order to obtain the energy-momentum dispersion. In our case we supply the wave packet with a momentum using the factor $e^{i\mathbf{k}_0\cdot\mathbf{r}_l}$, but do not specify energy. This can be thought of as a Bragg pulse with sharp momentum resolution but poor or nonexistent energy resolution. This allows us to explore various occupancies of the two energy bands.

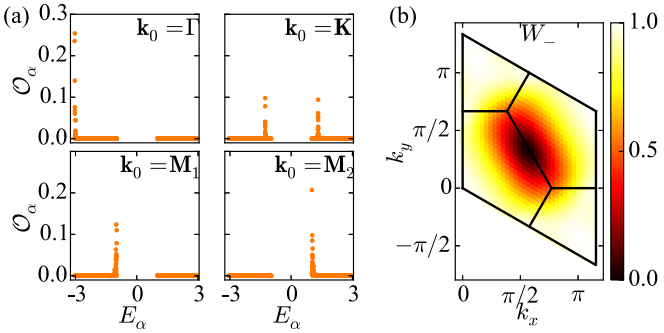

FIG. 2. (Color online) (a) Overlaps $\mathcal{O}_\alpha$ of the initial wave packet at different initial momenta $\mathbf{k}_0$ with the eigenstates of $\mathcal{H}_{\rm HM}$ (with periodic boundary conditions) plotted against the energy eigenvalues E_α. (b) Weight of the wave packet on the lower band (W_-) for each initial momentum in the Brillouin zone.

The momentum zero wave packet (2) turns out to predominantly have overlap with eigenstates of $\mathcal{H}_{\rm HM}$ at the bottom of the spectrum, in the lower band, as long as σ is not too small. This is generally true in simple lattice models with negative hopping constants. In a complicated model such as $\mathcal{H}_{\rm HM}$, this is not *a priori* obvious, but is the case for the parameters we are using.

Boosting the wave packet in momentum space as in Eq. (3) can result in the wave packet having support on both bands of $\mathcal{H}_{\rm HM}$. This is exemplified in Fig. 2 through the overlap of the wave packet with the eigenstates of $\mathcal{H}_{\rm HM}$. We denote the overlap of the initial state by $|\psi(t=0)\rangle$ with an eigenstate of $\mathcal{H}_{\rm HM}$ and $|u_\alpha\rangle$ with an eigenvalue E_α as $\mathcal{O}_\alpha = |\langle\psi(t=0)|u_\alpha\rangle|^2$. Figure 2(a) shows a plot of $\mathcal{O}_\alpha$ against E_α for four out of the six high-symmetry momentum points being the initial momentum of the wave packet. It can be seen that for $\mathbf{k}_0 = \mathbf{K}$ the wave packet has support on both bands. The wave packet corresponding to $\mathbf{k}_0 = \mathbf{M}_1$ is also shifted higher in energy, though it has overlaps primarily with the states of the lower band. On the contrary, for $\mathbf{k}_0 = \mathbf{M}_2$ the weight shifts almost entirely to the upper band. Such a drastic difference of behavior between the $\mathbf{M}_1$ and $\mathbf{M}_2$ points may seem unexpected because they are related by symmetry. However, the eigenfunction structures are of course inequivalent, so the overlap distributions after a momentum boost cannot be expected to be similar.

We quantify the weight of the wave packet on the lower band W_- by taking the sum of the overlaps of the wave packet with the eigenstates of the lower band. Mathematically,

$$W_- = \sum_{\alpha=1}^{N/2}\mathcal{O}_\alpha, \quad W_+ = 1 - W_-, \quad (4)$$

where W_+ is the weight on the upper band and N is the number of sites in the lattice and hence the number of single-particle eigenstates. The color map in Fig. 2(b) shows the magnitude

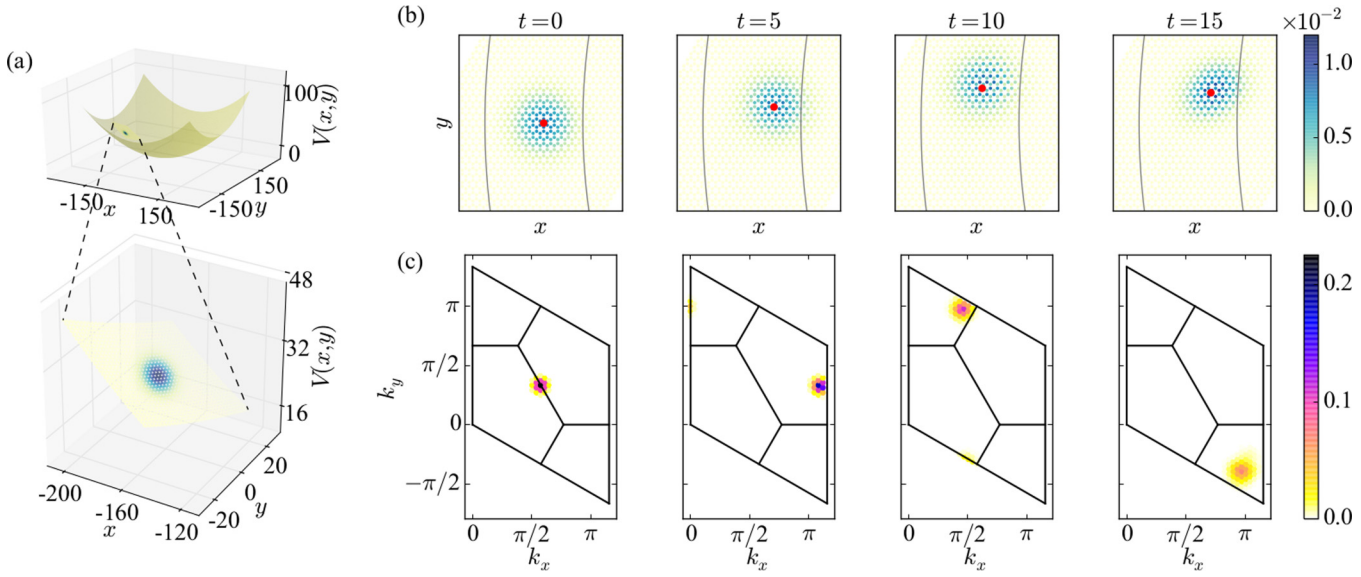

FIG. 3. (Color online) (a) Geometry of the lattice and the trap. The surface represents the potential of the harmonic trap and the colors show the occupancies of the wave packet at $t = 0$ on the real-space lattice. The lower figure shows a zoom near the wave packet. (b) Snapshots of the time evolution of the real-space occupancies $|c_l(t)|^2$. The red circle shows the center of the mass of the wave packet. The solid lines are equipotential contours of the trap potential. (c) Occupancies of each momentum mode in the Brillouin zone at different times ($|\tilde{c}_{\mathbf{k}}(t)|^2$). The trap strength for all figures is $V_0 = 0.002$. The initial wave packet has a Gaussian width $\sigma^2 = 50$, initial momentum $\mathbf{k}_0 = \mathbf{M}_2$, and $|\mathbf{r}_0 - \mathbf{r}_c| = 164.5$ in units of the lattice constant.

of W_- for a wave packet with a given initial momentum in the Brillouin zone.

C. Trap

The evolution in time is carried out with the Hamiltonian

$$\mathcal{H} = \mathcal{H}_{\rm HM} + \mathcal{H}_{\rm trap} = \mathcal{H}_{\rm HM} + \sum_l V(l)\hat{b}_l^\dagger \hat{b}_l, \tag{5}$$

where

$$V(l) = \frac{V_0}{2}|\mathbf{r}_l - \mathbf{r}_0|^2, \tag{6}$$

with $\mathbf{r}_0 = (x_0, y_0)$ denoting the center of the harmonic trap and V_0 controlling its strength. The force exerted by the trap is along the inward radial direction, so one expects Bloch oscillations in this direction. We are particularly interested in the transverse response and hence the angular velocity of the wave packet around the center of the trap is a natural observable to study. The angular variable θ at position $\mathbf{r} = (x, y)$ is given by $\theta = \tan^{-1}\frac{y-y_0}{x-x_0}$. Its average as a function of time is calculated using

$$\langle\theta\rangle(t) = \tan^{-1}\frac{\langle y\rangle(t) - y_0}{\langle x\rangle(t) - x_0} \tag{7}$$

from the averages x and y for the time-dependent wave functions

$$\langle x\rangle(t) = \sum_l |c_l(t)|^2 x_l, \quad \langle y\rangle(t) = \sum_l |c_l(t)|^2 y_l. \tag{8}$$

D. Simulations of wave-packet dynamics

In this work we present results for the exact dynamics of wave packets placed off center in the trap and compare them with semiclassical predictions. We present simulations mostly for a relatively weak trap ($V_0 = 0.002$), where the wave-packet width σ is much smaller than the distance ($\approx$164.5) to the trap center $\mathbf{r}_0$. The trap potential gradient (i.e., the force) does not vary too much over the extent of the wave packet. In Sec. V we also present results for a tighter trap ($V_0 = 0.02$), where the initial distance of the wave packet to the trap center is 10 times smaller so as to have the same force at the center of the wave packet. The trap curvature is more significant in this case.

In Fig. 3(b) we show the real-space evolution of the wave packet in the weak trap for two different initial momenta. We focus on dynamics up to $t \approx 20$. The motion of the wave packet on this time scale is not large compared to its width. The force acts in the radial (positive-x) direction. A transverse response, perpendicular to the force, is clearly visible; we analyze this quantitatively through the time dependence of $\langle\dot{\theta}\rangle$. In the following sections we provide a thorough comparison of numerically exact results for $\langle\dot{\theta}\rangle$ obtained through direct simulation (which we refer to as $\langle\dot{\theta}\rangle_{\rm exact}$) with predictions from the semiclassical formalism, to be defined below.

In addition to the transverse response, there are also Bloch oscillations in the radial direction; this is not obvious in the real-space snapshots but is more evident in momentum space. The motion of the wave packet in momentum space is obtained by taking a lattice Fourier transform of the coefficients $c_l(t)$ at each instant of time to obtain the occupancies of each momentum, denoted by $\tilde{c}_{\mathbf{K}}(t)$. This motion can be visualized by plotting the coefficients $|\tilde{c}_{\mathbf{k}}(t)|^2$ over the Brillouin zone at different instants of time, as done in Fig. 3(c). The wave packet moves through the Brillouin zone at constant rate in the direction of the force. Due to the periodicity of the Brillouin

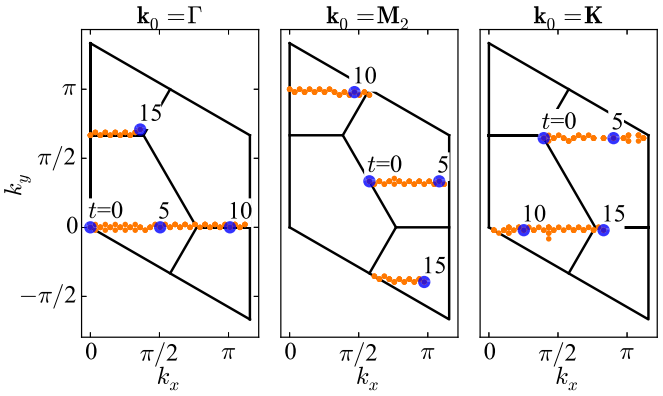

FIG. 4. (Color online) Trajectories of the wave packet in momentum space for three initial momenta showing Bloch oscillations. The orange circles represent the trajectory of the center of the wave packet in momentum space. The blue larger circles denote the position of the wave-packet center in momentum space at four instants of time ($t = 0$, 5, 10, and 15).

zone, each time the wave packet exits through the right or top boundary it reenters through the left or bottom boundary. As a visual aid, we show schematically in Fig. 4 the trajectories of the wave-packet centers starting from the three high-symmetry points.

III. SEMICLASSICAL DYNAMICS

In this section we set up the semiclassical framework to calculate the time evolution of $\dot{\theta}$(t). We first formulate the basic point-particle approach, under the standard assumption of simultaneously well-defined position and momentum. We then formulate an extension where the structure of the wave packet in momentum space is taken into account.

In the most basic semiclassical approach, the structure of the wave packet in both real and momentum space are ignored, so the wave packet or particle is described by a sharply defined position and momentum ($\mathbf{r}$,$\mathbf{k}$). In addition, it is also assumed that the wave-packet dynamics is completely governed by a single energy band. We will first write down the semiclassical equations with the assumption that the wave packet has support only on the lower band. The semiclassical equations of motion are [50]

$$\frac{d\mathbf{r}}{dt} = \nabla_{\mathbf{k}} E_-(\mathbf{k}) - \frac{d\mathbf{k}}{dt}\mathbf{\Omega}_-(\mathbf{k}), \tag{9a}$$

$$\frac{d\mathbf{k}}{dt} = \mathbf{F}. \tag{9b}$$

Here $E_-(\mathbf{k})$ is the energy dispersion and $\mathbf{\Omega}_-(\mathbf{k})$ is the Berry curvature of the lower band. From the second term in Eq. (9b) we see that the Berry curvature induces a velocity perpendicular to the direction of the external force, which leads to the transverse motion of the wave packet.

We now specialize to the geometry we are using, with a trapping potential centered at (x_0,y_0). Using (6), the external force is given by

$$\mathbf{F}(\mathbf{r}) = -\nabla_{\mathbf{r}} V(\mathbf{r}) = -V_0[(x - x_0)\hat{x} + (y - y_0)\hat{y}]. \tag{10}$$

So the semiclassical equations form a set of four coupled differential equations

$$v_{-,x}(\mathbf{k}) = \frac{dx}{dt} = \frac{\partial E_-(\mathbf{k})}{\partial k_x} + V_0(y - y_0)\Omega^z_-(\mathbf{k}), \tag{11a}$$

$$v_{-,y}(\mathbf{k}) = \frac{dy}{dt} = \frac{\partial E_-(\mathbf{k})}{\partial k_y} - V_0(x - x_0)\Omega^z_-(\mathbf{k}), \tag{11b}$$

$$\frac{dk_x}{dt} = -V_0(x - x_0), \tag{11c}$$

$$\frac{dk_y}{dt} = -V_0(y - y_0). \tag{11d}$$

This set of equations can be solved explicitly to trace out the trajectory in time of a particle in real and in momentum space. We label as $\langle\dot{\theta}\rangle_{-,\text{pp-sc}}$ the angular velocity corresponding to the real-space trajectories calculated in this way. (The subscript pp-sc stands for point-particle semiclassics and the minus sign denotes that the lower band properties have been used.) A similar calculation can be done with the characteristics of the upper band $E_+(\mathbf{k})$ and $\Omega^z_+(\mathbf{k})$ and the angular velocity so calculated is denoted by $\langle\dot{\theta}\rangle_{+,\text{pp-sc}}$.

As observed previously, wave packets can have support on both bands. One reasonable procedure would be to use the $\langle\dot{\theta}(t)\rangle_{-,\text{pp-sc}}$ or $\langle\dot{\theta}(t)\rangle_{+,\text{pp-sc}}$ curve, depending on whether the lower or upper band has more occupancy. We follow a somewhat more refined procedure by taking the weighted average of the two according to the weights $W_\mp$ of the initial packet on the two bands. Hence the angular velocity calculated from the point-particle semiclassics is defined as

$$\langle\dot{\theta}\rangle_{\text{pp-sc}} = W_-\langle\dot{\theta}\rangle_{-,\text{pp-sc}} + W_+\langle\dot{\theta}\rangle_{+,\text{pp-sc}}. \tag{12}$$

A key assumption above is that the wave packet can be treated like a point particle in both real and momentum space simultaneously, hence neglecting the quantum nature of the wave packet. However, in realistic quantum experiments and simulations, where the wave packet is of finite extent, the validity of this assumption is not *a priori* clear. We now extend this formalism to take into account the finite spread of the wave packet in momentum space. From the geometric definition $\theta = \tan^{-1}\frac{y-y_0}{x-x_0}$, we obtain

$$\dot{\theta} = \frac{(x - x_0)v_y - (y - y_0)v_x}{(x - x_0)^2 + (y - y_0)^2}. \tag{13}$$

By using the expressions of $v_{\pm,x}(\mathbf{k})$ and $v_{\pm,y}(\mathbf{k})$ obtained from Eqs. (11a) and (11b), we define the functions $\dot{\theta}_\pm(\mathbf{k})$ in the Brillouin zone. Their typical profiles are shown in Fig. 5, with parameter values corresponding to the initial position used in Fig. 3.

With our parameters, we have $E_-(\mathbf{k}) \approx -E_+(\mathbf{k})$. Also, we always have $\Omega_+(\mathbf{k}) = -\Omega_-(\mathbf{k})$. Hence we get $\dot{\theta}_-(\mathbf{k}) \approx -\dot{\theta}_+(\mathbf{k})$. In other words, the profiles shown in Fig. 5 for the two bands $\dot{\theta}_\pm(\mathbf{k})$ are nearly but not exactly negative of each other.

These profiles of $\dot{\theta}_\pm(\mathbf{k})$ can be used to calculate the evolution of the angular velocity in time by taking a weighted average of $\dot{\theta}_\pm(\mathbf{k})$, the weights being the occupancies of the wave function in momentum space ($|\tilde{c}_{\mathbf{k}}(t)|^2$) multiplied by the weights in each band $W_\pm$ defined in (4). We denote the angular velocity calculated this way by $\langle\dot{\theta}\rangle_{\text{wp-sc}}(t)$, the wp as a reminder

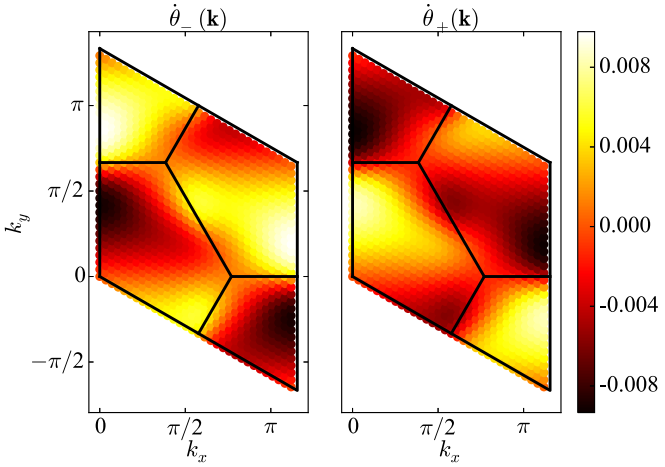

FIG. 5. (Color online) Profiles of $\dot{\theta}_-(\mathbf{k})$ and $\dot{\theta}_+(\mathbf{k})$ in the Brillouin zone as calculated from combining the semiclassical equations of motion (9b) and the kinematic relation (13). The coordinates of the center of the mass of the wave packet in real space relative to the center of the trap are given by $x - x_0 = -164.5$ and $y - y_0 = 0.5$ and the trap strength is $V_0 = 0.002$. Here $\dot{\theta}_-(\mathbf{k})$ and $\dot{\theta}_+(\mathbf{k})$ have nearly but not exactly equal and opposite values $\dot{\theta}_-(\mathbf{k}) \approx -\dot{\theta}_+(\mathbf{k})$.

that the wave-packet structure is taken into account. Thus

$$\begin{aligned}\langle\dot{\theta}(t)\rangle_{\text{wp-sc}} &= W_-\langle\dot{\theta}(t)\rangle_{-,\text{wp-sc}} + W_+\langle\dot{\theta}\rangle_{+,\text{wp-sc}} \\ &= W_-\sum_{\mathbf{k}\in\text{BZ}}|\tilde{c}_{\mathbf{k}}(t)|^2\dot{\theta}_-(\mathbf{k}) + W_+\sum_{\mathbf{k}\in\text{BZ}}|\tilde{c}_{\mathbf{k}}(t)|^2\dot{\theta}_+(\mathbf{k}) \\ &= \sum_{\mathbf{k}\in\text{BZ}}|\tilde{c}_{\mathbf{k}}(t)|^2[W_-\dot{\theta}_-(\mathbf{k}) + W_+\dot{\theta}_+(\mathbf{k})]. \qquad (14)\end{aligned}$$

This procedure assumes that the force does not change along the spatial extent of the wave packet; the spread of the wave packet in momentum space is taken into account while a point-particle description is used in real space. Therefore, this description will break down when the force varies significantly within the real-space support region of the wave packet (Sec. V). In addition, note that this is not a computationally advantageous approximation for the time evolution, since we are anyway solving the full problem in order to obtain the Fourier transform $\tilde{c}_{\mathbf{k}}(t)$. Our purpose here is to investigate whether (and how much) taking the momentum-space spread into account improves the semiclassical description.

In this work we focus on parameter regimes such that the wave packet does not have large displacements in real space within the time scales $t \lesssim 20$ of interest (Fig. 3). Therefore, we make a further simplifying assumption and take $\dot{\theta}$ as position independent, setting $\mathbf{r}$ to be the initial position of the wave packet at $t = 0$, and use the resulting distribution of $\dot{\theta}$ to calculate the average. In the following two sections we test how well this procedure describes the angular motion of the wave packet.

IV. COMPARISON OF SEMICLASSICAL PREDICTIONS WITH EXACT DYNAMICS

In this section we compare the angular velocities of the wave packet obtained from the exact simulations ($\langle\dot{\theta}\rangle_{\text{exact}}$) to those obtained from the semiclassical calculations ($\langle\dot{\theta}\rangle_{\text{pp-sc}}$ and $\langle\dot{\theta}\rangle_{\text{wp-sc}}$) and discuss the regimes of validity of the semiclassical framework. In Fig. 6 we plot the angular velocities as a function of time for the setup corresponding to that shown in Fig. 3(a) for two different sizes and three different initial wave-packet momenta Γ, $\mathbf{M}_2$, and $\mathbf{K}$. Before discussing in detail, we make some general observations.

(i) For the Γ point and $\mathbf{M}_2$ point initial states, $\langle\dot{\theta}\rangle_{\text{pp-sc}}$, calculated using the basic point-particle semiclassical equations (11), shows similar overall qualitative features as the evolution of the exact $\langle\dot{\theta}\rangle_{\text{exact}}$, but it generally fails to quantitatively reproduce the evolution. On the other hand, $\langle\dot{\theta}\rangle_{\text{wp-sc}}$, calculated using the modified semiclassics of Sec. III (taking into account the wave-packet structure in momentum space), reproduces many of the prominent features of the $\langle\dot{\theta}(t)\rangle_{\text{exact}}$ curve. For the $\mathbf{K}$ point initial state, there seems to be no noticeable agreement.

(ii) There is generally better agreement between the semiclassics and the exact evolution for the wave packet that is larger in real space ($\sigma^2 = 50$, top row) compared to the smaller wave packet ($\sigma^2 = 0.5$, bottom row).

(iii) For the larger wave packet ($\sigma^2 = 50$, top row), the Γ point initial state is almost completely in the lower band ($W_- = 0.999$) and the $\mathbf{M}_2$ point initial state is almost completely in the upper band ($W_+ = 0.985$). Hence, using only the lower band Γ or only the upper band $\mathbf{M}_2$ would give very nearly the same semiclassical curves as the ones shown, which are $W_\pm$-weighted mixtures.

For the smaller wave packet ($\sigma^2 = 0.5$, bottom row), the same is true with the Γ point initial state ($W_- = 0.99$), but the $\mathbf{M}_2$ point initial state now has a significant contribution from the lower band as well ($W_+ = 0.74$). This leads to cancellation of the weighted mixtures, so that, comparing Figs. 6(b) and 6(e), we see much smaller values of $\langle\dot{\theta}\rangle$ for the smaller wave packet. For the $\mathbf{K}$ point initial state, the contributions of the two bands largely cancel each other, resulting in tiny semiclassical predictions for $\langle\dot{\theta}(t)\rangle$.

We now discuss in more detail the larger ($\sigma^2 = 50$) wave packet Figs. 6(a)–6(c). A wave packet with zero initial momentum has support almost completely on the lower band ($W_- = 0.999$), hence the relevant profile of angular velocity is $\dot{\theta}_-(\mathbf{k})$. At the zero-momentum ($\Gamma$) point, both the gradient of the band dispersion and the Berry curvature in the lower band are zero, leading to a zero angular velocity. As a result, the wave packet starts with zero $\dot{\theta}$. From the momentum-space trajectory in Fig. 4(a) and the Brillouin zone profile of Fig. 5, one can infer that the wave packet mostly moves through regions of nearzero $\dot{\theta}$. As a result, the $\dot{\theta}$ remains relatively small, as can be seen in Fig. 6(a). The momentum-space shape of the packet plays a strong role in this case: As the trajectory lies roughly between positive and negative regions of $\dot{\theta}_-(\mathbf{k})$, small variations of the shape can cause $\dot{\theta}$ to vary between positive and negative values. Accordingly, the dynamics of $\langle\dot{\theta}(t)\rangle_{\text{exact}}$ is captured notably better by the extended semiclassics $\langle\dot{\theta}\rangle_{\text{wp-sc}}$ than by the point-particle approximation $\langle\dot{\theta}\rangle_{\text{pp-sc}}$.

As discussed in Sec. II B, the wave packet with initial momentum at $\mathbf{M}_2$ has support almost entirely on the upper band ($W_- = 0.015$), hence the upper band characteristics are more relevant here. At the $\mathbf{M}_2$ point, although the gradient of the band dispersion vanishes, the Berry curvature has a sharp peak [see Fig. 1(c)]. As a result, the wave packet gains a finite angular velocity almost immediately at $t \approx 0$. (Note that

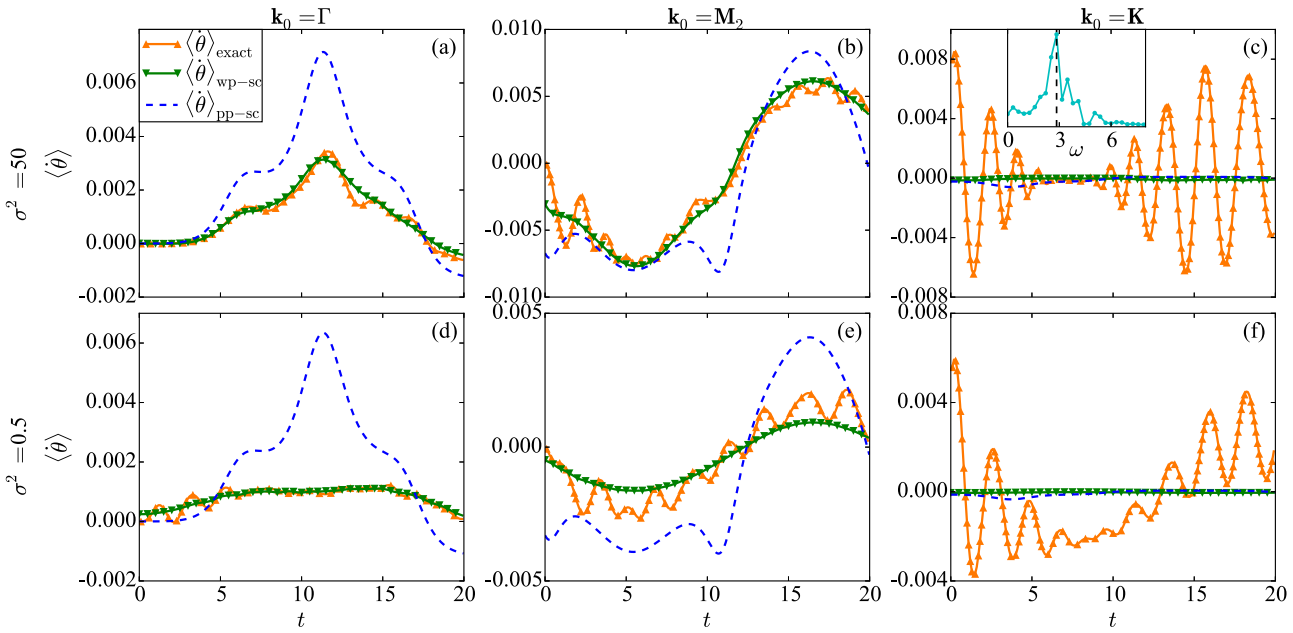

FIG. 6. (Color online) Angular velocity from exact simulations $\langle\dot\theta\rangle_{\rm exact}$, compared with point-particle semiclassics $\langle\dot\theta\rangle_{\rm pp\text{-}sc}$ and with extended semiclassics taking the momentum-space structure into account $\langle\dot\theta\rangle_{\rm wp\text{-}sc}$. The initial wave-packet size (a)–(c) $\sigma^2 = 50$ and (d)–(f) $\sigma^2 = 0.5$. Three different initial momenta are shown: (a) and (d) $\mathbf{k}_0 = \Gamma$, (b) and (e) $\mathbf{k}_0 = \mathbf{M}_2$, and (c) and (f) $\mathbf{k}_0 = \mathbf{K}$. For $\mathbf{k}_0 = \Gamma$ and $\mathbf{k}_0 = \mathbf{M}_2$, $\langle\dot\theta\rangle_{\rm wp\text{-}sc}$ agrees quantitatively with $\langle\dot\theta\rangle_{\rm exact}$, whereas $\langle\dot\theta\rangle_{\rm pp\text{-}sc}$ shows qualitative agreement at best. For $\mathbf{k}_0 = \mathbf{K}$, $\langle\dot\theta\rangle_{\rm exact}$ shows oscillations that are not captured by semiclassics. In (c) the Fourier transform of the oscillations in $\langle\dot\theta\rangle_{\rm exact}$ is shown in the inset.

the semiclassical approximations, by construction, start with nonzero $\dot\theta$ at $t = 0$, which is the value of $\dot\theta$ at the $\mathbf{M}_2$ point. The physical or exact $\dot\theta$ starts at zero.) Considering the trajectory Fig. 4(b) and the Brillouin zone profile of Fig. 5, we note that the trajectory moves through regions of large $\dot\theta$; this is reflected in the larger absolute values of Fig. 6(b). The trajectories in momentum space intersect regions of $\dot\theta_+(\mathbf{k}) < 0$ for $t \lesssim 10$ to explore regions $\dot\theta_+(\mathbf{k}) > 0$ at later times. The change of sign can be seen in Fig. 6(b) in all three curves.

For the wave packet with $\mathbf{k}_0 = \mathbf{K}$, the dynamics of $\langle\dot\theta\rangle_{\rm exact}$ shows pronounced oscillations, which preclude meaningful comparison with the semiclassical predictions. The oscillations are due to the fact that the initial state created according to Eq. (3) has significant weight on both lower and upper bands ($W_- = 0.457$), with a relatively-well-defined energy gap between eigenstates occupied in the lower band and eigenstates occupied in the upper band. This can be seen through the overlaps plotted in Fig. 2(a). A Fourier transform of the $\langle\dot\theta(t)\rangle_{\rm exact}$ [Fig. 6(c) inset] shows that the dominant frequency (peak around $\approx$2.8 with width $\approx$0.3) matches the energy difference ($\approx$2.6) between eigenstates of high overlap [Fig. 2(a), top right]. The weighted band averages shown as semiclassical predictions stay near zero, which could be thought of as the value around which the exact $\langle\dot\theta(t)\rangle_{\rm exact}$ oscillates, but it is currently unclear whether this is a coincidence. It is also currently unclear whether a more sophisticated way of incorporating multiple bands might allow the semiclassics to reproduce the oscillatory behavior or the average curve around which $\langle\dot\theta(t)\rangle_{\rm exact}$ oscillates.

In Figs. 6(d)–6(f) we have used an initial wave packet with $\sigma^2 = 0.5$. The Gaussian wave packet is centered at the center of a hexagon in real space, so that even with such a small σ there are six sites equally occupied. The exact $\langle\dot\theta(t)\rangle_{\rm exact}$ now deviates significantly from the point-particle semiclassics $\langle\dot\theta\rangle_{\rm pp\text{-}sc}$. The extended semiclassics $\langle\dot\theta\rangle_{\rm wp\text{-}sc}$ continues to describe the overall behavior for the Γ point and $\mathbf{M}_2$ point initial states. The exact dynamics now shows oscillations for all three initial momenta. This can be understood through the overlap distribution, shown in Fig. 7. For the smaller packet, the overlaps are spread out more in energy and also are far more biased toward more equal occupancies of the two bands (W_- values are closer to $\frac{1}{2}$ compared to the corresponding values for the bigger packet). As a result, interference oscillations are visible also for the Γ point and $\mathbf{M}_2$ point initial states [Figs. 7(d) and 7(e)].

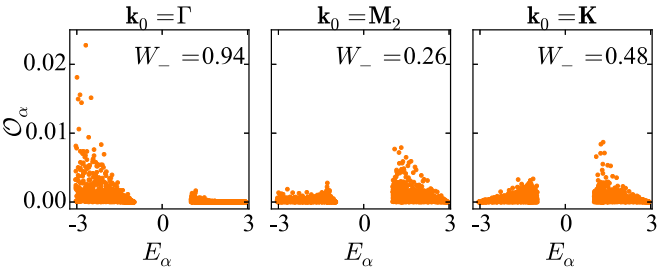

FIG. 7. (Color online) Overlaps as in Fig. 2(a), for a smaller wave packet $\sigma^2 = 0.5$. Compared with the case of $\sigma^2 = 50$ [Fig. 2(a)], this smaller wave packet has a much more spread-out distribution of weights on the eigenstates of $\mathcal{H}_{\rm HM}$. The weight of the wave packets in the lower band W_- (provided in each panel) are all closer to 1/2 compared to the larger wave packet of Fig. 2, where we had $W_- = 0.999$, 0.015, and 0.457 for these three momenta.

V. SEMICLASSICS IN A TIGHT TRAP

In Sec. IV we showed that, as the spread of the initial wave packet in real space is made bigger, the agreement between the results from the semiclassical approximations and exact simulations improves. The idea is that, increasing size in real space corresponds to decreasing size in momentum space (as reflected also in decreasing spread in energy space); thus the point-particle approximation in momentum space is more justified. However, increasing real-space size can also lead to violation of semiclassics, as the semiclassical equations of motion also assume sharply defined position. One effect is that the finite spread of the wave packet in real space could lead to different potential gradients (different forces) at different points within the wave packet. This effect would not play a role for a constant gradient but can occur in a harmonic trap. This kind of tidal force makes the point-particle notion less justified in real space.

In order to characterize this effect, we consider the geometry of Fig. 8(a) with $V_0 = 0.02$, one order of magnitude stronger than that in Fig. 3. The distance between the center of the trap and the center of the wave packet is adjusted such that the force at the center of the wave packet remains the same as the geometry shown in Fig. 3(a). It can be seen from Fig. 8(a) that, in the course of time evolution, the wave packet breaks apart, spreads out, and does not keep the notion of a well-defined wave packet as compared to the shallower trap (Fig. 3). This is also reflected in the evolution of the wave packet in momentum space as shown in Fig. 8(b). For time scales similar to those studied in previous sections, the wave packet in momentum space gets distorted and diffuses completely, unlike the case in Fig. 3(c) where there is still a notion of a well-defined peak centered around some value of momentum. Quite surprisingly, our semiclassical calculation does not seem to fail completely even in this extreme case since $\langle\dot{\theta}\rangle_{\text{wp-sc}}$ and $\langle\dot{\theta}\rangle_{\text{exact}}$ still agree qualitatively (see Fig. 8). Even the point-particle semiclassics $\langle\dot{\theta}\rangle_{\text{pp-sc}}$ reproduces qualitatively some of the peaks and dips of the exact curve. As in previous cases, for $\mathbf{k}_0 = \mathbf{K}$ there are strong oscillations due to occupancies in both bands.

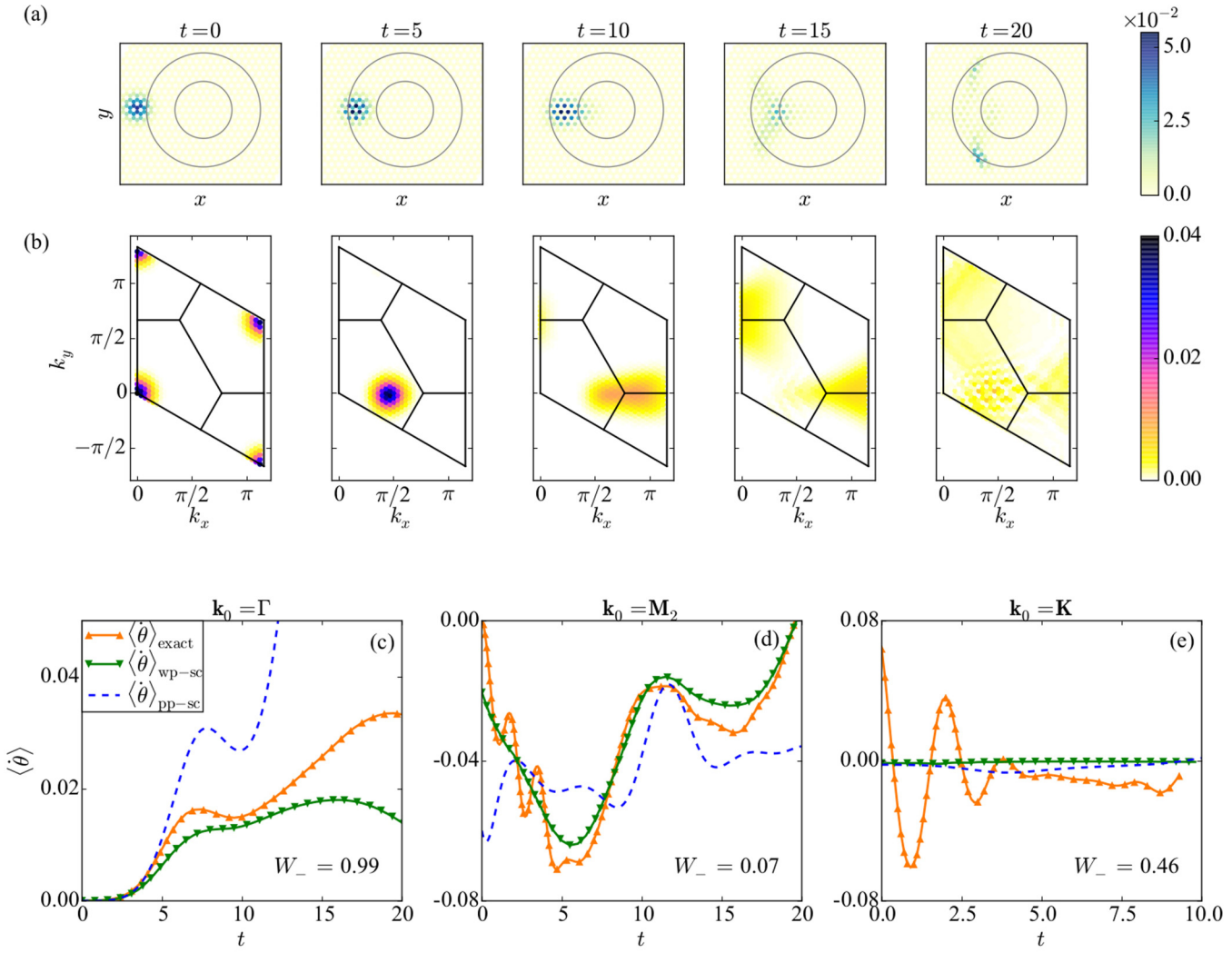

FIG. 8. (Color online) Dynamics in a tight trap, with $V_0 = 0.02$, initial position $|\mathbf{r}_0 - \mathbf{r}_c| = 16.45$, and initial size $\sigma^2 \approx 10$. (a) and (b) Snapshots for $\mathbf{k}_0 = \Gamma$. (a) Real-space occupancies $|c_l(t)|^2$. Solid lines are equipotential contours of the trap potential. (b) Corresponding momentum space occupancies $|\tilde{c}_{\mathbf{k}}(t)|^2$ in the Brillouin zone. (c) Comparison between the angular velocities calculated from full simulations $\langle\dot{\theta}\rangle_{\text{exact}}$ with the two types of semiclassics $\langle\dot{\theta}\rangle_{\text{pp-sc}}$ and $\langle\dot{\theta}\rangle_{\text{wp-sc}}$.

VI. SUMMARY AND DISCUSSION

In this work we have explored the dynamics of a Gaussian wave packet, with and without initial crystal momentum, on the Haldane honeycomb Chern-band lattice in the presence of external forces provided by a harmonic potential. We have focused on short-time dynamics and compared to semiclassical treatments. Semiclassical descriptions of wave-packet dynamics are obviously appealing, but the range of applicability is poorly explored. This work can be regarded as a step toward obtaining detailed information on the regimes of validity of the semiclassical manner of predicting trajectories. We have formally treated single-particle dynamics, but our considerations should be applicable to noninteracting Bose condensates and approximately to weakly interacting Bose condensates.

We have found that the point-particle semiclassics reproduces many qualitative features even for wave functions that are quite small in real space and hence extended over non-negligible portions of the Brillouin zone. When this momentum-space extent is taken into account, the agreement can be excellent even when the point-particle approximation fails. This shows that the basic idea of semiclassics, following position and momentum simultaneously, can correctly embody quantum dynamics even when the point-particle approach fails. Using a tight trap, we have also shown that this extended semiclassical approach can function reasonably even when the wave packet is completely distorted or even torn apart (Fig. 8). While this is reassuring for the philosophy behind semiclassics, it does not immediately lead to a computationally advantageous approximation, since to obtain the momentum-space structure we first evolved the complete system in time (i.e., solved the problem computationally). However, one can envision an extended semiclassics where the wave packet in momentum space is assumed to have fixed shape and the center moves according to the point-particle equations (9).

This study was directly motivated by recent developments such as the experimental realization of Haldane's honeycomb model in a cold-atom system [13], the experimental and theoretical interest in the response of a localized wave packet to an applied force (potential gradient) [13,22,27,29,44], and recent theoretical studies of dynamics in various backgrounds using semiclassics [29,54,56,58–62]. In two-dimensional lattices, a potential gradient will of course lead to Bloch oscillations in the gradient direction (as widely studied, e.g., in [62–65,65–68]), but may also induce a transverse response. This can happen even without Berry curvature [62], simply due to the structure of the energy band. In the presence of Berry curvature, the transverse response occurs due to a combination of the two effects.

The present study opens up many new questions. First, we have focused on time scales such that the wave-packet displacements are of the order of the wave-packet size. It remains an open question to see how well semiclassics works when the trajectories are long compared to the wave-packet size. For example, Refs. [29,54] have predicted a dramatic turning point in the trajectory of a wave packet traveling through a honeycomb (graphene) lattice with a constant potential gradient. It is unclear how closely a finite-sized quantum wave packet would follow such a prediction, especially when the position dynamics couples to internal distortion dynamics of a realistic wave packet. Second, it remains an open question whether some version of our extended semiclassics can be fashioned into a computationally useful approximation scheme. Third, our treatment of multiple-band occupancies is rather primitive (an incoherent average) and is unable to account for interference oscillations. Clearly, development of multiple-band semiclassics for such time-evolution phenomena, perhaps along the lines of Ref. [59], is called for. Finally, since cold-atom experiments are more likely to track interacting Bose condensates or fermionic clouds rather than single-particle wave packets, it is of interest to find out in which situations the dynamics of many-fermion and many-boson clouds resemble single-particle wave-packet dynamics.

ACKNOWLEDGMENTS

M.H. thanks A. Eckardt and C. Groß for useful discussions.

APPENDIX: MOMENTUM SPACE PROPERTIES OF THE HALDANE MODEL

The semiclassical equations of motion (9) take the gradient of the energy dispersion and the Berry curvature in momentum space as input. In this Appendix we give some details of these momentum-space properties of the Haldane model, for completeness. Being realized on a lattice with a two-site basis, the Haldane model Hamiltonian in momentum space can be written as a collection of 2×2 Hamiltonians $h(\mathbf{k})$:

$$\mathcal{H}_{\mathrm{HM}} = \sum_{\mathbf{k}\in BZ} \Psi_{\mathbf{k}}^{\dagger} h(\mathbf{k}) \Psi_{\mathbf{k}}, \tag{A1}$$

with

$$h(\mathbf{k}) = \sigma^0 B^0(\mathbf{k}) + \boldsymbol{\sigma} \cdot \mathbf{B}(\mathbf{k}), \tag{A2}$$

where $\Psi_{\mathbf{k}}^{\dagger} = (\hat{b}_{A,\mathbf{k}}^{\dagger}, \hat{b}_{B,\mathbf{k}}^{\dagger})$ and $\hat{b}_{A(B),\mathbf{k}}^{\dagger}$ creates a Bloch state with momentum $\mathbf{k}$ on sublattice $A(B)$. The σ's are Pauli matrices with σ^0 being the identity matrix. We label the vectors connecting the nearest-neighbor sites as $\mathbf{a_1} = (0, -1)$, $\mathbf{a}_2 = (\sqrt{3}/2, 1/2)$, and $\mathbf{a}_3 = (-\sqrt{3}/2, 1/2)$ and the vectors connecting the next-nearest neighbors as $\mathbf{b}_1 = \mathbf{a}_2 - \mathbf{a}_3$, $\mathbf{b}_2 = \mathbf{a}_3 - \mathbf{a}_1$, and $\mathbf{b}_3 = \mathbf{a}_1 - \mathbf{a}_2$. With this notation, B_0 and $\mathbf{B}$ turn out to be

$$B_0(\mathbf{k}) = 2J_2 \cos\phi \sum_{i=1}^{3} \cos \mathbf{k} \cdot \mathbf{b}_i, \tag{A3a}$$

$$B_x(\mathbf{k}) = J_1 \sum_{i=1}^{3} \cos \mathbf{k} \cdot \mathbf{a}_i, \tag{A3b}$$

$$B_y(\mathbf{k}) = J_1 \sum_{i=1}^{3} \sin \mathbf{k} \cdot \mathbf{a}_i, \tag{A3c}$$

$$B_z(\mathbf{k}) = -2J_2 \sin\phi \sum_{i=1}^{3} \sin \mathbf{k} \cdot \mathbf{b}_i. \tag{A3d}$$

The energy dispersions of the two bands are

$$E_{\pm}(\mathbf{k}) = B_0(\mathbf{k}) \pm |\mathbf{B}(\mathbf{k})|^2, \tag{A4}$$

where $+$ $(-)$ denotes the upper (lower) band.

The eigenstates of the Hamiltonian (A2) for a given momentum $\mathbf{k}$ can be written as

$$u_{+,\mathbf{k}} = \begin{pmatrix} e^{-i\frac{\zeta_{\mathbf{k}}}{2}} \cos\frac{\eta_{\mathbf{k}}}{2} \\ e^{+i\frac{\zeta_{\mathbf{k}}}{2}} \sin\frac{\eta_{\mathbf{k}}}{2} \end{pmatrix}, \quad u_{-,\mathbf{k}} = \begin{pmatrix} e^{-i\frac{\zeta_{\mathbf{k}}}{2}} \sin\frac{\eta_{\mathbf{k}}}{2} \\ -e^{+i\frac{\zeta_{\mathbf{k}}}{2}} \cos\frac{\eta_{\mathbf{k}}}{2} \end{pmatrix}, \tag{A5}$$

where $\eta_{\mathbf{k}}$ and $\zeta_{\mathbf{k}}$ are defined via

$$\eta_{\mathbf{k}} = \cos^{-1}\frac{B_z(\mathbf{k})}{|\mathbf{B}(\mathbf{k})|}, \quad \zeta_{\mathbf{k}} = \tan^{-1}\frac{B_y(\mathbf{k})}{B_x(\mathbf{k})}. \tag{A6}$$

With this notation, the Berry curvature is given by

$$\Omega_{\pm} = \mp\frac{1}{4\pi}\epsilon_{\mu\nu}[\partial_{k_\mu}\cos\eta_{\mathbf{k}}][\partial_{k_\nu}\zeta_{\mathbf{k}}], \tag{A7}$$

where $\epsilon_{\mu\nu}$ is the two-dimensional Levi-Cività symbol and $\Omega_{-\,(+)}$ refers to the Berry curvature of the lower (upper) band.

[1] M. Z. Hasan and C. L. Kane, Rev. Mod. Phys. **82**, 3045 (2010).
[2] X.-L. Qi and S.-C. Zhang, Rev. Mod. Phys. **83**, 1057 (2011).
[3] F. D. M. Haldane, Phys. Rev. Lett. **93**, 206602 (2004).
[4] F. D. M. Haldane, Phys. Rev. Lett. **61**, 2015 (1988).
[5] C. L. Kane and E. J. Mele, Phys. Rev. Lett. **95**, 226801 (2005).
[6] B. A. Bernevig, T. L. Hughes, and S.-C. Zhang, Science **314**, 1757 (2006).
[7] M. König, S. Wiedmann, C. Brüne, A. Roth, H. Buhmann, L. W. Molenkamp, X.-L. Qi, and S.-C. Zhang, Science **318**, 766 (2007).
[8] M. König, H. Buhmann, L. W. Molenkamp, T. Hughes, C.-X. Liu, X.-L. Qi, and S.-C. Zhang, J. Phys. Soc. Jpn. **77**, 031007 (2008).
[9] C.-Z. Chang, J. Zhang, X. Feng, J. Shen, Z. Zhang, M. Guo, K. Li, Y. Ou, P. Wei, L.-L. Wang *et al.*, Science **340**, 167 (2013).
[10] M. Aidelsburger, M. Atala, M. Lohse, J. T. Barreiro, B. Paredes, and I. Bloch, Phys. Rev. Lett. **111**, 185301 (2013).
[11] H. Miyake, G. A. Siviloglou, C. J. Kennedy, W. C. Burton, and W. Ketterle, Phys. Rev. Lett. **111**, 185302 (2013).
[12] T. Uehlinger, G. Jotzu, M. Messer, D. Greif, W. Hofstetter, U. Bissbort, and T. Esslinger, Phys. Rev. Lett. **111**, 185307 (2013).
[13] G. Jotzu, M. Messer, R. Desbuquois, M. Lebrat, T. Uehlinger, D. Greif, and T. Esslinger, Nature (London) **515**, 237 (2014).
[14] N. Goldman, I. Satija, P. Nikolic, A. Bermudez, M. A. Martin-Delgado, M. Lewenstein, and I. B. Spielman, Phys. Rev. Lett. **105**, 255302 (2010).
[15] X.-J. Liu, X. Liu, C. Wu, and J. Sinova, Phys. Rev. A **81**, 033622 (2010).
[16] T. D. Stanescu, V. Galitski, and S. Das Sarma, Phys. Rev. A **82**, 013608 (2010).
[17] M. Buchhold, D. Cocks, and W. Hofstetter, Phys. Rev. A **85**, 063614 (2012).
[18] D.-L. Deng, S.-T. Wang, and L.-M. Duan, Phys. Rev. A **90**, 041601 (2014).
[19] A. R. Kolovsky, F. Grusdt, and M. Fleischhauer, Phys. Rev. A **89**, 033607 (2014).
[20] M. Killi and A. Paramekanti, Phys. Rev. A **85**, 061606 (2012).
[21] M. Killi, S. Trotzky, and A. Paramekanti, Phys. Rev. A **86**, 063632 (2012).
[22] A. Dauphin and N. Goldman, Phys. Rev. Lett. **111**, 135302 (2013).
[23] P. Hauke, M. Lewenstein, and A. Eckardt, Phys. Rev. Lett. **113**, 045303 (2014).
[24] L. D'Alessio and M. Rigol, Nat. Commun. **6**, 8336 (2015).
[25] M. D. Caio, N. R. Cooper, and M. J. Bhaseen, Phys. Rev. Lett. **115**, 236403 (2015).
[26] N. Goldman, J. Dalibard, A. Dauphin, F. Gerbier, M. Lewenstein, P. Zoller, and I. B. Spielman, Proc. Natl. Acad. Sci. USA **110**, 6736 (2013).
[27] M. Aidelsburger, M. Lohse, C. Schweizer, M. Atala, J. Barreiro, S. Nascimbene, N. Cooper, I. Bloch, and N. Goldman, Nat. Phys. **11**, 162 (2015).
[28] P. D. Sacramento, Phys. Rev. E **90**, 032138 (2014).
[29] H. M. Price and N. R. Cooper, Phys. Rev. A **85**, 033620 (2012).
[30] A. G. Grushin, S. Roy, and M. Haque, arXiv:1508.04778.
[31] L. Lu, J. D. Joannopoulos, and M. Soljačić, Nat. Photon. **8**, 821 (2014).
[32] F. D. M. Haldane and S. Raghu, Phys. Rev. Lett. **100**, 013904 (2008).
[33] S. Raghu and F. D. M. Haldane, Phys. Rev. A **78**, 033834 (2008).
[34] J. Koch, A. A. Houck, K. Le Hur, and S. Girvin, Phys. Rev. A **82**, 043811 (2010).
[35] M. Hafezi, E. A. Demler, M. D. Lukin, and J. M. Taylor, Nat. Phys. **7**, 907 (2011).
[36] A. Petrescu, A. A. Houck, and K. Le Hur, Phys. Rev. A **86**, 053804 (2012).
[37] Z. Wang, Y. Chong, J. Joannopoulos, and M. Soljačić, Nature (London) **461**, 772 (2009).
[38] K. Fang, Z. Yu, and S. Fan, Nat. Photon. **6**, 782 (2012).
[39] M. C. Rechtsman, J. M. Zeuner, Y. Plotnik, Y. Lumer, D. Podolsky, F. Dreisow, S. Nolte, M. Segev, and A. Szameit, Nature (London) **496**, 196 (2013).
[40] M. Hafezi, S. Mittal, J. Fan, A. Migdall, and J. Taylor, Nat. Photon. **7**, 1001 (2013).
[41] R. Matsumoto and S. Murakami, Phys. Rev. Lett. **106**, 197202 (2011).
[42] R. Matsumoto and S. Murakami, Phys. Rev. B **84**, 184406 (2011).
[43] R. Shindou, R. Matsumoto, S. Murakami, and J.-i. Ohe, Phys. Rev. B **87**, 174427 (2013).
[44] L. Duca, T. Li, M. Reitter, I. Bloch, M. Schleier-Smith, and U. Schneider, Science **347**, 288 (2015).
[45] M.-C. Chang and Q. Niu, Phys. Rev. Lett. **75**, 1348 (1995).
[46] M.-C. Chang and Q. Niu, Phys. Rev. B **53**, 7010 (1996).
[47] G. Sundaram and Q. Niu, Phys. Rev. B **59**, 14915 (1999).
[48] T. Jungwirth, Q. Niu, and A. H. MacDonald, Phys. Rev. Lett. **88**, 207208 (2002).
[49] P. Gosselin, F. Ménas, A. Bérard, and H. Mohrbach, Europhys. Lett. **76**, 651 (2006).

[50] D. Xiao, M.-C. Chang, and Q. Niu, Rev. Mod. Phys. **82**, 1959 (2010).
[51] D. Xiao, Y. Yao, Z. Fang, and Q. Niu, Phys. Rev. Lett. **97**, 026603 (2006).
[52] N. A. Sinitsyn, J. Phys.: Condens. Matter **20**, 023201 (2008).
[53] A. M. Dudarev, R. B. Diener, I. Carusotto, and Q. Niu, Phys. Rev. Lett. **92**, 153005 (2004).
[54] R. B. Diener, A. M. Dudarev, G. Sundaram, and Q. Niu, arXiv:cond-mat/0306184.
[55] E. van der Bijl and R. A. Duine, Phys. Rev. Lett. **107**, 195302 (2011).
[56] H. M. Price and N. R. Cooper, Phys. Rev. Lett. **111**, 220407 (2013).
[57] P. T. Ernst, S. Götze, J. S. Krauser, K. Pyka, D.-S. Lühmann, D. Pfannkuche, and K. Sengstock, Nat. Phys. **6**, 56 (2010).
[58] J. M. Pruneda and I. Souza, Phys. Rev. B **79**, 045127 (2009).
[59] D. Culcer, Y. Yao, and Q. Niu, Phys. Rev. B **72**, 085110 (2005).
[60] C. Wickles and W. Belzig, Phys. Rev. B **88**, 045308 (2013).
[61] G. Pettini and M. Modugno, Phys. Rev. A **83**, 013619 (2011).
[62] J. M. Zhang and W. M. Liu, Phys. Rev. A **82**, 025602 (2010).
[63] A. R. Kolovsky and H. J. Korsch, Phys. Rev. A **67**, 063601 (2003).
[64] D. Witthaut, F. Keck, H. J. Korsch, and S. Mossmann, New J. Phys. **6**, 41 (2004).
[65] S. Mossmann, A. Schulze, D. Witthaut, and H. J. Korsch, J. Phys. A **38**, 3381 (2005).
[66] H. Trompeter, W. Krolikowski, D. N. Neshev, A. S. Desyatnikov, A. A. Sukhorukov, Y. S. Kivshar, T. Pertsch, U. Peschel, and F. Lederer, Phys. Rev. Lett. **96**, 053903 (2006).
[67] L. Tarruell, D. Greif, T. Uehlinger, G. Jotzu, and T. Esslinger, Nature (London) **483**, 302 (2012).
[68] T. Uehlinger, D. Greif, G. Jotzu, L. Tarruell, T. Esslinger, L. Wang, and M. Troyer, Eur. Phys. J. Spec. Top. **217**, 121 (2013).